Development of non-cryogenic neutrino tracking detectors: *A measurement of the time resolution of MCP-based photodetectors*

Alexander Vostrikov
Supervisor: Henry Frisch

May 21, 2012

Abstract

There is a set of problems associated with neutrino physics: mass hierarchy, CP violation, the Majorana/Dirac nature and leptogenesis. All of these require extremely precise measurements. We are interested in developing a new type of non-cryogenic tracking detector with high timing resolution. Understanding the resolution required from the detector is part of the experimental process. I have made analytical calculations and helped to build a Geant4 framework for simulations of the experiment to estimate the resolution. The next step was to determine what resolution one can get experimentally. We created a testing facility at Argonne National Laboratory (ANL) to determine the time resolution of MCP-based photodetectors used Large-Area Picosecond Photo-Detectors (LAPPD) technology. I am part of the group taking data at the facility. I have performed data analysis and compared the data to analytical calculations and results of simulations. The results show feasibility of creation of $1 \times 1 \times 4$ m detector, which is able to determine muon sign using 500 gauss magnetic field.

Table of contents

Chapter 1

Introduction

1.1 Neutrino physics questions: mass hierarchy, CP violation, the Majorana/Dirac nature and leptogenesis

The value of quark CP violation cannot explain the ratio between matter and antimatter in the universe. Leptogenesis [1] is the generic term for hypothetical physical processes that produced an asymmetry between leptons and antileptons in the very early universe, resulting in the dominance of leptons over antileptons. Studying this process involves neutrino interaction research.

There are variety of models introducing neutrino mass [2]. For example, the Dirac model explains neutrino oscillations between the light neutrinos. The Majorana equation requires for a particle to be its own antiparticle, which also can be valid for neutrinos. Besides, there is a hypothetical type of neutrino that do not interact via any of the fundamental interactions of the Standard Model except gravity (sterile neutrinos).

1.2 The Large-Area Picosecond Photo-Detectors (LAPPD) Project

LAPPD collaboration aims to develop large-area systems to measure the time-of-arrival of relativistic particles with sub-nanosecond resolution [3]. The ultimate goal is 1 picosecond resolution. This is a factor 100 better than the present state-of-the-art.

The project involves development in a number of areas. One of them is multi–channel plate (MCP) photo-detectors. MCP is a set of parallel channels — electron multipliers. MCP acts similar to a regular photo multiplier, but its dynode structure is continuous. A stack of two MCP allows electron multiplication factor of about 10^6 and high time resolution.

Another part of LAPPD project is effective extracting of time from MCP signal. An MCP testing facility was built in Argonne National Laboratory (ANL). It is shown that time resolution of MCP-based detectors depends on the method of time extraction and the background to signal ratio. The goal of this work is to reach 10 picosecond timing resolution using stack of two 8" square MCP.

1.3 Motivation for designing a new kind of detector

To address stated above neutrino physics questions precise measurements in the neutrino experiments are required. One of the possibilities to improve the data quality is charge and momentum definition of the muons created from neutrino interactions.

Professor Henry Frisch within LAPPD collaboration suggested an experiment which is going to provide the possibility to make this type of measurements. The experiment is called Daniel Boone (in honor of Daniel Boone [4] and the series of Boone experiments at Fermilab [5]). It represents a 4 m^3 water tank (Figure 1.1) surrounded by high resolution picosecond photo-detectors based on MCP technologies [6]. The detectors register light radiated by muons, which allows reconstructing a trajectory of a muon in the water.

If the water tank is put into a constant magnetic field, muons trajectories are curved. Measuring the curvature of the trajectories gives the muons charge sign and momentum. This is possible if the resolution of the detectors is enough. That is why one needs to estimate the necessary resolution of the detectors and compare it with real resolution.

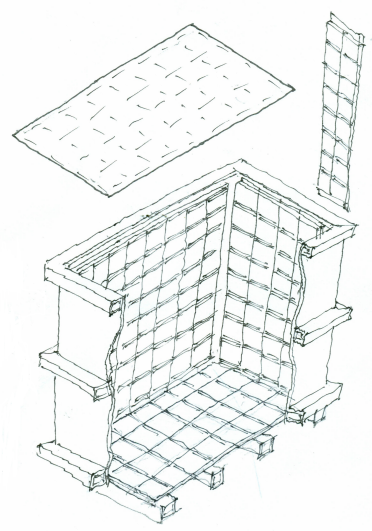

Figure 1.1: A sketch of the detector for Daniel Boone experiment. 4 m^3 water tank is surrounded by MCP-based photo-detectors. The detectors represents stacks of two MCP 8" × 8" size. These stacks cover whole or partial surface area of the water tank.

This work is a part of LAPPD project. My personal impact in the project is analytical calculations, building Geant4 simulation framework together with Andrey Elagin, development of software for data taking and data analysis, participation in testing facility setup, data taking and data analysis together with Bernhard Adams, Andrey Elagin, Razib Obaid, Matthew Wetstein.

In Chapter 2 we consider muon motion in water to estimate resolution necessary for muon charge determination. In Chapter 3 the testing facility at ANL is described. In Chapter 4 the process of measuring signal from MCP detectors is presented. In Chapter 5 of the paper we provide the latest results of timing resolution measurements.

Chapter 2

What resolution is needed for sign determination of neutrino induced muons?

2.1 Sign determination

The standard method to determine the sign of charge of a particle is to place it into a constant magnetic field. If a particle of charge q moves in the constant magnetic field $\vec{B}$ with the velocity $\vec{v}$, it experiences force

$$\vec{F} = q\left[\vec{v}, \vec{B}\right]. \tag{2.1}$$

One can see that if the magnetic field and the velocity direction are known, direction of the force depends on the sign of charge q. Thus, deflection of the particle's trajectory from the straight line in the constant magnetic field determines the sign of charge of the particle.

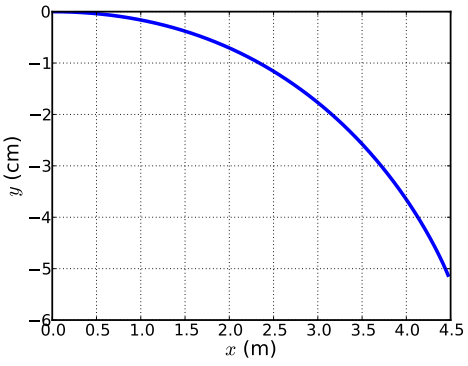

Figure 2.1: The muon trajectory in water in the constant magnetic field $B = 100$ gauss. The initial kinetic energy of the muon is 1 GeV. The initial direction of motion is towards the positive x-axis from the origin. The charge of the muon is positive. The magnetic field is directed towards the positive z-axis. The muon energy loss rate in water is 2 MeV/cm and it does not depend on energy in this energy range.

2.2 Analytical calculations

Analytical calculations of the muon's motion in water are shown in Appendix A. When the muon loses energy in water with the rate independent on its energy, equations of motion can be solved analytically. This solution does not include multiple scattering effect. The trajectory of the positive charged muon with initial kinetic energy 1 GeV in the constant magnetic field of 100 gauss is shown in Figure 2.1. One can see that when the muon

travels almost 4.5 m in the direction of the initial motion (this is the traveled distance of muon with energy 1 GeV in water), the deflection from this direction due to the magnetic field is about 5 cm only. The ability to measure this deflection is essential for the muon sign determination.

To describe necessary resolution one needs to introduce term sagitta (Figure 2.2). If there is a curve trajectory L from point A to point B then its sagitta s is defined as the maximum distance from the straight line AB and points of the curve trajectory:

$$d = \max_{a \in L} D(a, AB), \tag{2.2}$$

where $D(a, AB)$ is distance between point a and line AB.

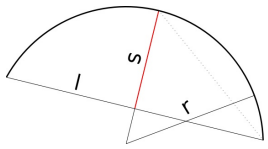

Figure 2.2: Sagitta definition for a circle trajectory. l is the straight line, r is the radius, s is the sagitta.

The sagitta dependence on the strength of magnetic field and traveled distance can be calculated analytically. The results of the calculations are shown on Figure 2.3. One can see that for the studied range of parameters the sagitta depends linearly on the magnetic field and quadratically on the traveled distance.

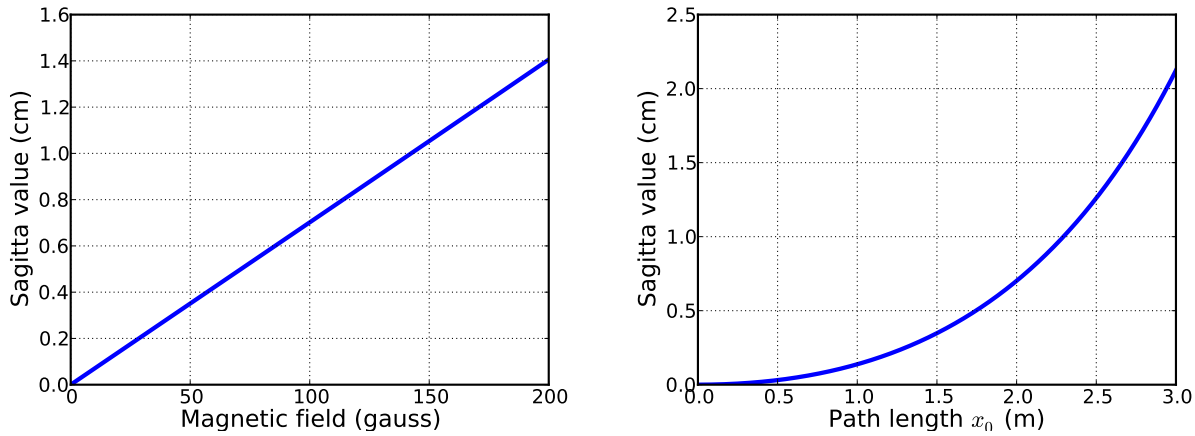

Figure 2.3: Sagitta of the muon trajectory dependence on the magnetic field strength (left plot) and the traveled distance (right plot). For the left plot the traveled distance is fixed at 2 m. For the right plot the magnetic field strength is 100 gauss. The plots show that for successful muon sign reconstruction in the 2 m long detector using the 100 gauss magnetic field one needs a resolution better than 7 mm.

Initial suggestion for the detector size was $1 \times 2 \times 2$ m. One can see from the Figure 2.3 that if the muon travels 2 m in the detector and the external magnetic field is 100 gauss, the sagitta is 7 mm. Increasing of the magnetic field and the detector longitudinal size increases the sagitta which improves resolution. Muon multiple scattering makes resolution worse. That is why the next step of the experiment analysis is simulation which includes muon multiple scattering.

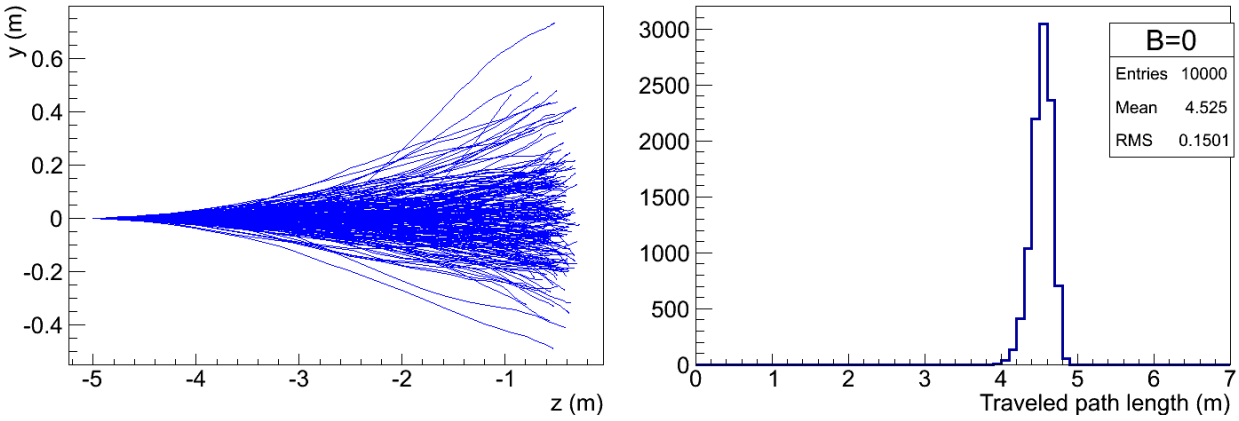

Figure 2.4: The muons' tracks in water with multiple scattering without the magnetic field (on the left plot). Muons start from the point $y = 0$, $z = 5$ m. Their velocity directed towards the positive z-axis. The initial energy is 1 GeV. The final point of the track is where the muon stops. The muons' traveled path length (on the right plot). The average traveled path length is about 4.5 m.

2.3 Simulations

The purpose of the simulations is to see an effect of muon multiple scattering on the trajectories and to define an optimal size of the detector and necessary for the resolution magnetic field strength.

The Geant4 simulation framework is created for this purpose. A rectangular water tank of different sizes can be simulated. The muon multiple scattering effect is added to the muon motion features. The magnetic field strength can be controlled.

The origin of the coordinate system is located at the center of the water tank. The coordinate axes are perpendicular to the walls. The water tank size is $L_x \times L_y \times L_z$, where L_i is the length along the i-axis, $i = x, y, z$. The muon of energy 1 GeV initially simulated at the intersection of the tank wall and the negative z-axis. Its velocity directed towards the positive z-axis. The magnetic field is applied along the x-axis.

Without multiple scattering muons would move along the straight line at the zero magnetic field. During the motion they would loose the energy from 1 GeV to zero. When multiple scattering is taken into account the trajectories are curved. On the left plot of Figure 2.4 the muons' tracks are shown. The water tank size here chosen large enough for muons not leaving water. Distribution of the muon traveled path length in water is shown on the right plot of Figure 2.4. The traveled path length is about 4.5 m.

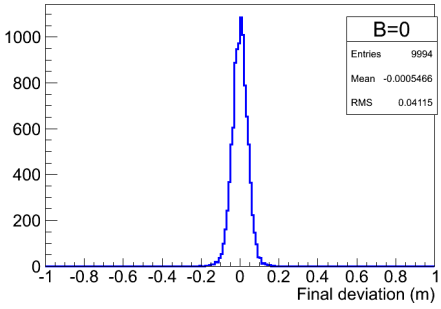

Figure 2.5: Distribution of the transverse coordinate of the muons after 2 m traveled distance in water. Multiple scattering is applied. The external magnetic field is zero. The average value of the coordinate is zero, the standard deviation is about 41 mm.

For the design parameters determination two different options of the detector size are con-

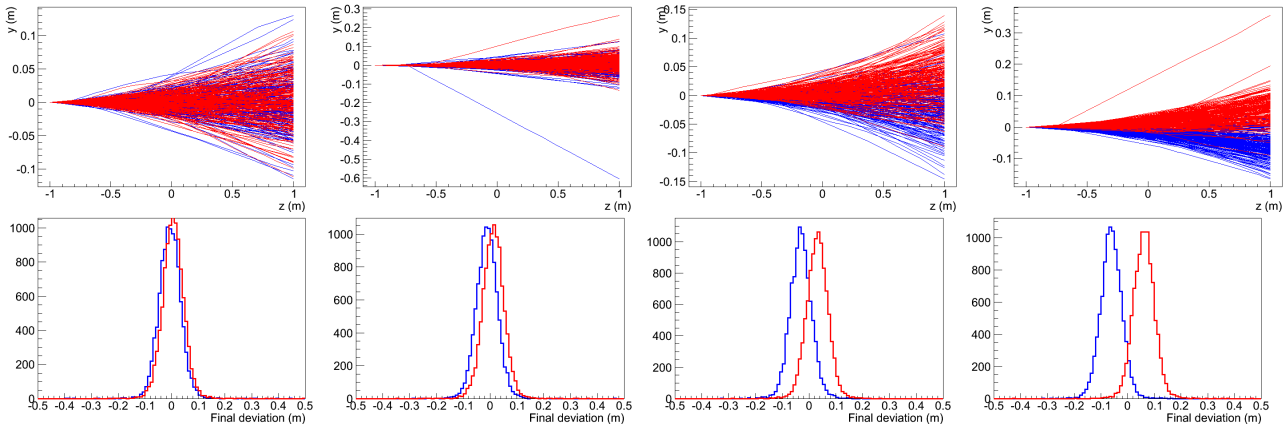

Figure 2.6: The simulation results for the $1 \times 2 \times 2$ m detector. There are muons tracks in the detector presented at the top row of the plots in the (y, z) plane. Muons start from the wall of the detector with the initial energy 1 GeV and the velocity directed towards the positive z-axis. The initial transverse coordinates of the muons are $x = 0$ and $y = 0$. The magnetic field is applied along the x-axis in its positive direction. That is why tracks are deflected in the y-axis direction. At the bottom row of the plots distributions of the y coordinate of the muons at the exit from the detector (final deviation) is shown. The magnetic field strength is 100, 200, 500 and 1000 gauss for the first, second, third and forth columns of the plot correspondingly. The positive muons are shown in red. The negative muons are shown in blue.

sidered: the initial suggestion $1 \times 2 \times 2$ m and the extended length option $1 \times 1 \times 4$ m. The latter option has increased length. Thus the muon can travel longer distance in water what increases the sagitta and has a positive impact on the sign determination.

The results of the simulations for the first and the second options are shown in Figures 2.6 and 2.7 correspondingly. On the top row of the plots there are muons' tracks. The tracks from the positive charged muons are shown in red. The tracks from the negative charged muons are shown in blue. Different values of the magnetic field applied to the water tank are 100, 200, 500 and 1000 gauss — first, second, third and fourth columns respectively. One can see that the significant separation of muons and antimuons for 2 m long detector is achieved at the 1 kgauss magnetic field. For the 4 m long detector the significant separation is observed at the

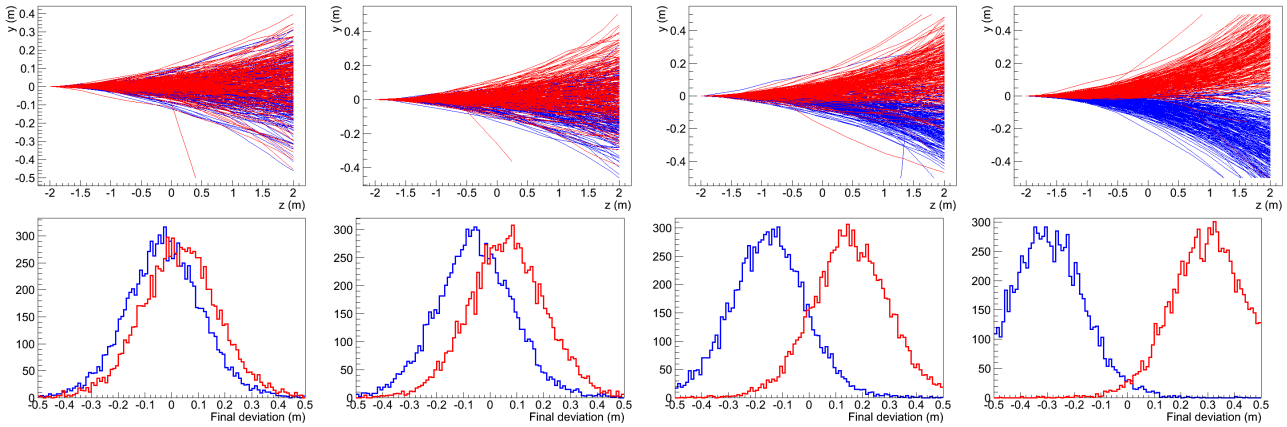

Figure 2.7: The simulation results for the $1 \times 1 \times 4$ m detector. See description in Figure 2.6

500 gauss magnetic field.

It is necessary to describe this separation numerically. The initial velocity of the muon is parallel to the z-axis. The magnetic field is parallel to the x-axis. It means that we expect deviation of the muon trajectory in the y direction. (That is the reason why we plot the muons' tracks in the (y, z) plane.) If there is no magnetic field and multiple scattering, the muon's y coordinate at the exit of the water tank is zero. When there is multiple scattering, but there is no magnetic field, the expected value of the y coordinate at the exit is zero (see Figure 2.5). When the magnetic field is on and $\vec{B}$ is directed towards the positive x-axis, according to Equation (2.1) the positive muons tend to deflect in the positive y-axis direction, the negative muons tend to deflect in the negative y-axis direction. One can use the coordinate y at the exit of the water tank — the final deviation — to describe the muon sign separation.

On the bottom rows in Figures 2.6 and 2.7 there are plots of the final deviation distributions for each case of the magnetic field strength and the detector length. Each plot has two distributions. The positive muon distribution is in red, the negative muon distribution is in blue. The greater magnetic field, the bigger separation between the peaks. Moreover, one can notice that separation for the 4 m long detector is bigger than for the 2 m long detector, but the peaks in the $1 \times 2 \times 2$ m case are sharper.

Table 2.1: Separation of muons and antimuons. Different cases of the detector length L_z and magnetic field B are presented. Graphically the results are presented in Figures 2.6 and 2.7.

Case	μ^+		μ^-		Separation	
	μ, mm	σ, mm	μ, mm	σ, mm	$\Delta\mu$, mm	$\Delta\mu/\bar{\sigma}$
2 m, 100 gauss	6.0	40.75	-6.2	41.85	12.2	0.30
2 m, 200 gauss	12.0	41.72	-11.8	40.68	23.9	0.58
2 m, 500 gauss	30.3	42.17	-31.0	42.02	61.4	1.49
2 m, 1000 gauss	61.3	41.19	-61.3	39.99	122.6	3.00
4 m, 100 gauss	30.4	144.8	-27.7	141.9	58.2	0.39
4 m, 200 gauss	61.7	143.6	-57.0	143.9	118.7	0.80
4 m, 500 gauss	150.0	140.3	-148.8	139.0	298.8	2.00
4 m, 1000 gauss	280.7	124.6	-278.2	125.0	558.9	3.75

Summary of the simulations results is presented in Table 2.1. Separation of the peaks growths linearly with the magnetic field. The average RMS width of the peaks in the 2 m long detector is about 40 mm. The average RMS width of the peaks in the 4 m long detector is about 140 mm what is 3.5 times bigger. In spite of this, separation of the peaks in terms of the standard deviation for the $1 \times 1 \times 4$ m detector is bigger. It reaches 3.75 for the 1 kgauss magnetic field. For the $1 \times 2 \times 2$ m detector this ratio is equal to 3 for the 1 kgauss magnetic field.

Another important characteristic to select the size of the detector is constancy of emitted photons' Cherenkov angle. MCP-based detectors cover the water tank and collect Cherenkov light radiated by muons from neutrino decay. Muon emits cones of light when travels in water.

The angle of the cones is called Cherenkov angle θ and can be found as

$$\cos\theta = \frac{c}{nv}, \tag{2.3}$$

where n is refraction coefficient of water and v is muon speed. If the angle is approximately constant during the flight, then muon's trajectory can be reconstructed by collected light. That is why muon should not loose too much energy in the water tank.

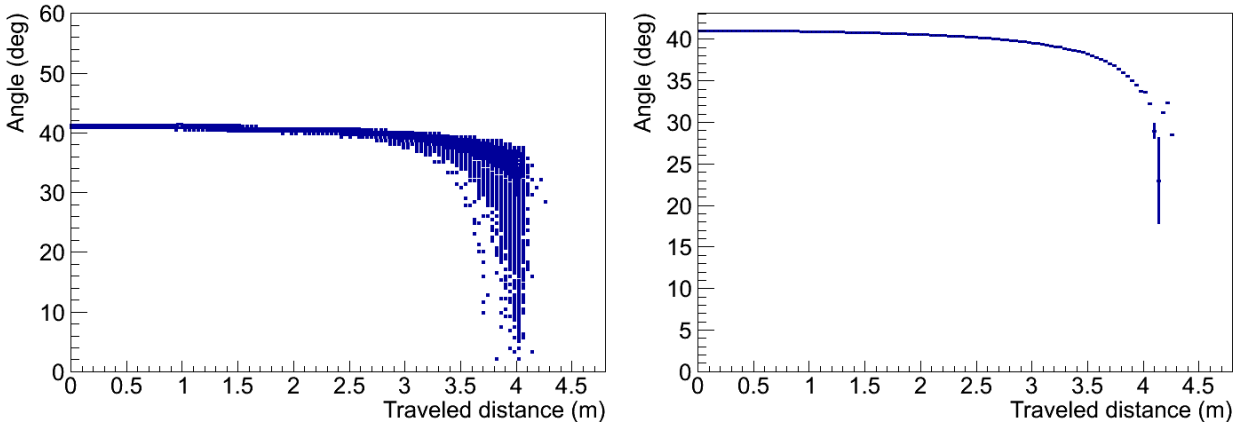

Figure 2.8: Cherenkov angle distribution (on the left) and the average Cherenkov angle (on the right) of emitted photons dependence on muon's traveled distance for the detector with $L_z = 4$ m and magnetic field 1 kgauss. Cherenkov angle drops down significantly after 2.5 m of distance. This would make muon track reconstruction more complicated.

Cherenkov angle distribution and the average Cherenkov angle dependence on traveled distance are shown in Figure 2.8. One can see that Cherenkov angle does not change on first 2.5 m of muon's flight. After that muon's kinetic energy becomes small enough for speed to be different from speed of light significantly. This will make track reconstruction more complicated in 4 m long detector.

Here we consider a muon created on the wall of the detector. In reality neutrinos decay in the random point inside the detector. That is why traveled distance of the muons in 4 m long detector is smaller than 4 m in average. This means that muons motion will happen at constant speed if they are born close enough to the center of the water tank. Besides, even if the muon travels more than 2.5 m, intensity of Cherenkov radiation reduces after that. That is why extra length of the detector will not negatively effect the muon tracking.

Chapter 3

Experimental apparatus

The experimental apparatus for this work is a testing facility built in Argonne National Laboratory in terms of LAPPD project. Ti:Saph laser creates infrared beam. Then using BBO crystals we can transform it into ultraviolet beam with wavelength about 800 nm. This beam splits into two parts: one of them goes directly to the oscilloscope's trigger channel, another one goes to the vacuum chamber (Figure 3.1).

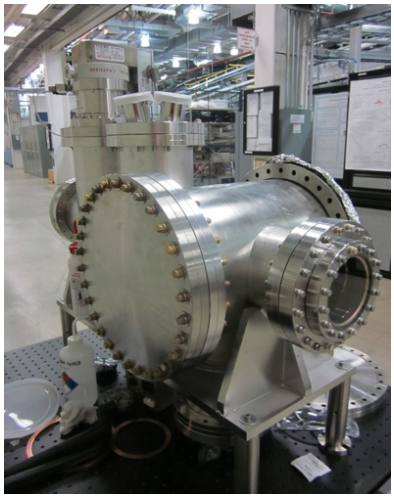

Figure 3.1: 8" vacuum chamber. Laser beam goes to the chamber through the window on the right. MCP-based detector setup inside the chamber as shown in Figure 3.2.

The vacuum chamber has a setup inside, which is shown in Figure 3.2a. UV light goes to the window of the chamber, reflects from the mirror and incidents a specific point of the photocathode (PC). PC is the first element of the stack of MCP (Figure 3.2b). Actual intensity of the laser beam is very high, but for the particular setup we use filters making the system works in single photon regime. When a photon acts on PC, it emits an electron from the other side. Under PC there is a stack of two MCP and an anode (Figure 3.2c). PC, top and bottom of both MCP and the anode are connected to high-voltage source. The electron emitted from PC is accelerated by the potential difference between PC and top of first MCP. Interacting with MCP the electron causes secondary emission elections. They are accelerated by the potential differences. Thus, multiple amplification of the signal occurs, and the avalanche of the electrons hits the anode.

The anode represents an array of parallel strips (Figure 3.2c). When an electron hits a strip, it creates a signal which spreads to both ends of the strip. Measuring the signal arrival time on both ends of the strip one can determine the position of the hit along the strips. When the avalanche of the electrons hits the anode, it can hit one or more strips (depending on transverse size of the avalanche). Besides, cross-talk signals occur on the neighboring strips. Measuring the amplitude of the signal on each strip one can determine the position of the hit perpendicular to the strips.

In this work we are concentrated on resolution along the strips. Using the optics we create a hit at the specific point of the anode such that only a few strips collect the signal.

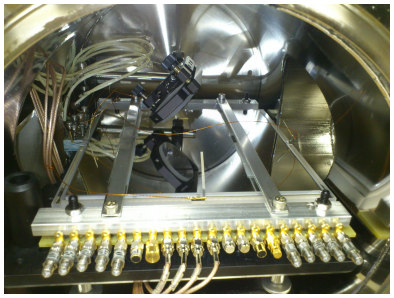

(a) MCP-based detector setup inside the vacuum chamber. The mirror directs the laser beam to the photocathode (PC). PC, two MCP and the anode are connected to the high-voltage source. The anode strips are connected to the oscilloscope.

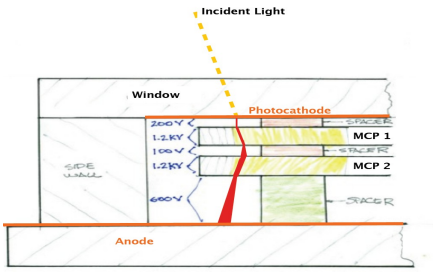

(b) MCP stack setup. UV light incidents PC, which emits electrons. The electrons form the avalanche in MCP due to secondary emission electrons. The avalanche hits the anode and create a signal.

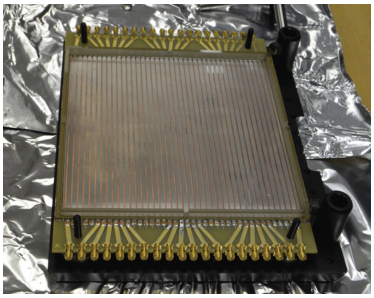

(c) Anode. It consists on parallel strips, which collect the signal. When an electron hits a strip, the signal forms and spreads towards two ends of the strip. The ends of the strip are connected with the oscilloscope, which receives the signals.

Figure 3.2: Setup of the testing MCP-based detector in the vacuum chamber.

These strips are connected to the oscilloscope, which already has a trigger signal. Thus, the oscilloscope has a signal from trigger and signals from the anode. There is an example in Figure 3.3 of the pulses measured by the oscilloscope. Trigger channel is shown in purple, signals from the opposite ends of one strip are shown in yellow and blue. One can see that signals from different ends of the strip arrive in different time. This time difference provides us with information about position of the hit along the strip.

The goal of the experiment is to extract time from the pulses precisely enough to have time difference resolution better than 10 ps. This is done by reducing electronics noise, increasing the amplitude of the signal and improving algorithms of time extraction from the pulse.

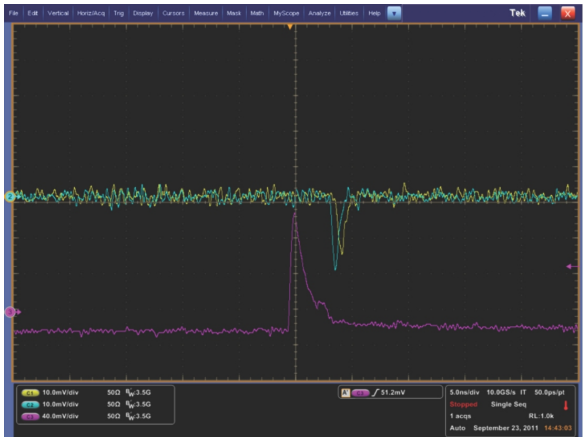

Figure 3.3: An example of the oscilloscope reading. There is a trigger channel in purple. Channels which collect signal from the opposite ends of an anode's strip are shown in yellow and blue. There is a hit on the strip, that is why both ends have clear peaks. The peaks are separated in time. This time difference can be converted to the position of the hit along the strip.

Chapter 4

Data taking

4.1 Data acquisition

In the experiment data is collected by the oscilloscope. The oscilloscope has four channels and its sampling rate is 10 Gs/s. This means that time resolution of the oscilloscope is 100 ps.

One of the channel is used for triggering. As it is described in Chapter 3, the trigger sends a signal to oscilloscope before the signal on MCP is formed. This tells oscilloscope to start reading the data from other channels and save them during the following 1 ms. This set of data is called a frame.

The other two channels are connected to the opposite ends of the anode's strip. This strip is selected to be the one which collects all the signal from MCP. Let us call this strip an active strip. These two channels define the resolution of the detector.

The last channel connected to one and of the neighboring strip. This will be useful for cross-talk analysis.

The oscilloscope is operated by a computer script. The script sets parameters of the detector, tells the oscilloscope to read a number of frames (usually 5000 or 10000) and save this data on the oscilloscope's hard drive. The data is saved in RAW format.

4.2 Parameter monitoring

The script sets voltages on PC, top and bottom of both MCP, and the anode. It makes a scan on the voltages and saves the data in different directories.

Why do we need the parameter monitoring? Potential difference between PC and the top of first MCP determines the energy which emitted electron has hitting the MCP. Amount of secondary emitted electrons depends on this energy. The voltages across MCP define the acceleration of the secondary emitted electrons. The angle of the cone which electrons go from the first to the second MCP depends on the potential difference between the MCP. This defines how many pores electrons go in the second MCP. To make resolution better one wants all the electrons go to as few pores as possible. The electron avalanche size on the anode depends on the voltage between the bottom of the second MCP and the anode.

All these factors affect the resolution. We change them in specific ranges defined by the properties of MCP to find the best option for the resolution.

Chapter 5

Resolution of LAPPD detectors

5.1 Quality cuts

The oscilloscope saves the data in RAW format. The data contains frames from trigger, two ends of the anode's strip and one end of the neighboring strip. There is a MATLAB script which converts RAW format data to MAT format. This data is analyzed by script "analysis".

The first step of the script is application of quality cuts. We have to check that both ends of the active strip have a significant pulse. Besides, trigger channel needs to have significant amplitude to make sure that the oscilloscope is triggered correctly. The script defines the offset of each channel of the oscilloscope. Then it defines amplitude of the signal and selects the events which satisfy the required quality cuts.

5.2 Extracting the time from the waveform

Another function of the script is extracting pulses from the frame. If there are more than one pulse on the active strip, the event is rejected. There is exactly one pulse per channel from the active strip in the selected events. At this point the script extracts time from these pulses using different techniques.

The simplest method to extract the time is absolute threshold. There is a preset threshold and the time when the signal crosses this threshold called time of the pulse. This method is simple, but it has a disadvantage: timing depends on the amplitude of the signal. That is why script "analysis" does not use this method.

5.2.1 Constant fraction discriminator (CFD)

The script extracts time using improved method — constant fraction discriminator (CFD). CFD does not have a preset threshold, but it has a preset fraction. Threshold is defined as this fraction of the amplitude of the signal. The script builds spline of the pulse with 1 ps step. The first point of the spline above the threshold defines timing of the pulse. This approach determines time which does not depend on the amplitude of the signal. We chose the fraction to be 50%.

5.2.2 Fitted CFD

There is the following improvement of CFD implemented to the script. The improvement is called fitted CFD. It allows to improve timing due to smoothing of background noise effects. The difference of this method from the regular CFD is that threshold and timing are defined from the fit of the rising edge of a pulse but not the pulse itself. We applied the Gaussian fit to the rising edge of the pulse.

5.2.3 Measurements

A number of MCP was used in the measurements. For each pair of MCP we did the voltage scan and then defined the optimal parameters for better resolution. Then we did a position scan, when we changed a position of the laser spot at PC, thus changing a position of the hit along the strip. For each position we extracted time of pulses on each end of the active strip for each frame. Then we calculated the difference of these times ΔT. Finally for each position we calculated the average value of ΔT.

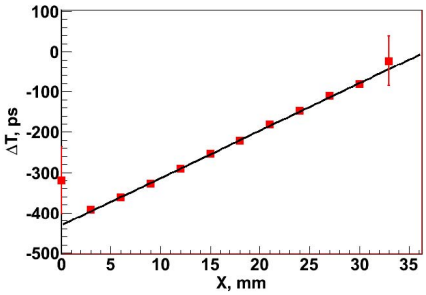

Figure 5.1: Pulses time difference on opposite ends of the active strip dependence on the laser beam position.

The average ΔT dependence on X — position of the laser beam spot for one of the MCP pairs is shown in Figure 5.1. As expected ΔT depends linearly on X. The slope of the graph is 10 ps/mm, which corresponds to speed of signal propagation through the anode strip line 2/3 of the speed of light. This measurement confirms that measured timing has physical meaning. The next step is resolution measurements.

5.2.4 Measured resolution

To determine the resolution one needs to consider a fixed position of the laser beam. There is set of events for this position. Each event gives time difference ΔT. If position of the laser beam is fixed ΔT should not change, but in reality if we plot a distribution of ΔT over set of events, we have a Gaussian distribution. RMS of this distribution is defined as resolution.

There are corresponding distributions for one of the measurements in Figure 5.2. Two approaches of timing measurement are applied: CFD (Figure 5.2a) and fitted CFD (Figure 5.2b). CFD method provides resolution of 11.9 ps, which is very close to our goal, but fitted CFD technique gives us resolution of 9.2 ps, which corresponds our initial goal of 10 ps resolution. The best resolution achieved at this moment is better than 6 ps.

5.3 Analysis of systematic and statistical uncertainties

We did the resolution measurements for number of sets of MCP and different settings of the laser and noise reduction system. All of them gave us different values of resolution, what was necessary to explain. It was discovered that time resolution depends on the ratio of back-

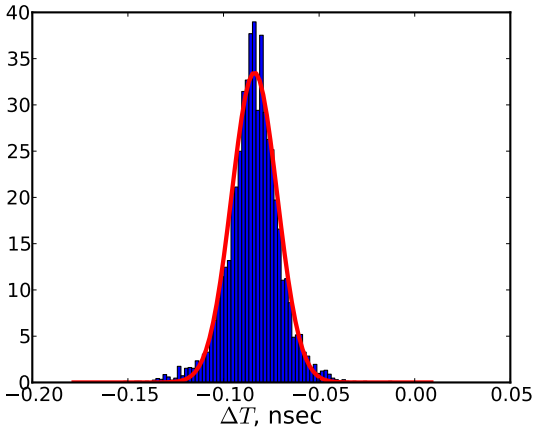

(a) CFD timing. Resolution is 11.9 ps.

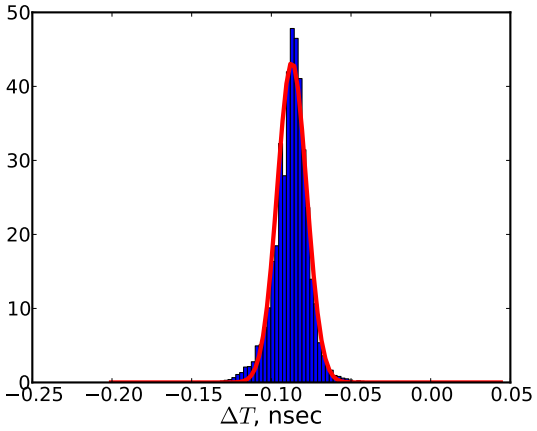

(b) Fitted CFD timing. Resolution is 9.2 ps.

Figure 5.2: Distributions of ΔT — difference between time of the pulses at opposite ends of the active strip.

ground noise to the pulse amplitude linearly (Figure 5.3). To check this observation we made a simulation.

The simulation program generates a pulse with Gaussian rising edge of the amplitude 1. The width of the signal is the same as the real one. Then the program generates random noise with amplitude a and add this noise to the pulse. Finally, the program extracts timing from the generated signal. Different values of a in range $[0, 0.1]$ are considered. The result of the simulation is shown in Figure 5.3.

Difference between simulation and real can be explained by the laser beam spot size. The signal is generated exactly in the same time in the simulation when in reality there is finite size beam spot.

The noise suppression activity has already improved resolution significantly. The LAPPD group will continue to improve signal to noise ratio for better resolution results.

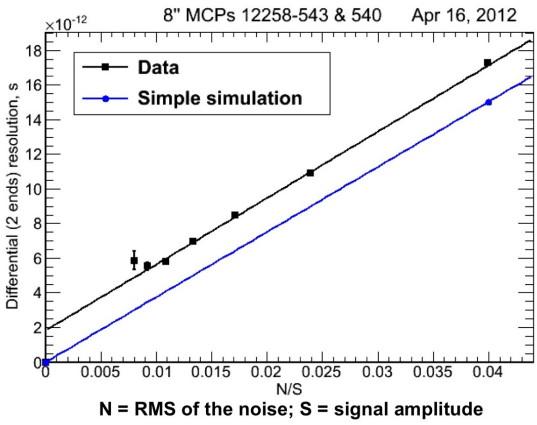

Figure 5.3: Resolution dependence on background noise. Simulation results are shown in blue. Real data are shown in black. Dependences are linear. Displacement is explained by the laser beam spot size, which is not included in the simulation.

Chapter 6

Conclusions

This work is a basement of new kind of detector. Necessary characteristics of the detector calculated analytically and using the Geant4 framework developed together with Andrey Elagin. The detector of size $1 \times 1 \times 4$ m is shown to be optimal. The longest dimension of the detector should be oriented along the beam line. External magnetic field of 500 gauss is necessary for muon sign determination. Space resolution of the order of 7 mm is required.

The biggest part of the work is LAPPD technology development and MCP-based detectors resolution measurements. I participated in setup of the testing facility at ANL and data taking. This includes optics setup, detector positioning in the vacuum chamber, high-voltage connections and connections between anode and the oscilloscope. I developed an interface between the laboratory computer and the oscilloscope for collecting data automatically and parameter monitoring. I developed script "analysis" and simulation program for noise effect analysis. I participated in data analysis and noise reduction actions. Finally, LAPPD group demonstrated timing resolution better than 6 ps and noise effect on the resolution. This corresponds to 600 μm spacial resolution.

Obtained results allow to conclude that building of proposed Daniel Boone experiment is feasible. High resolution MCP-based detectors will be able to resolve muon sign with appropriate magnetic field.

The results are presented at Fast-timing meeting at ANL and at LAPPD group meeting. Development of the MCP-based detectors will be continued in terms of LAPPD program.

I would like to say thank you to Bernhard Adams, Andrey Elagin, Razib Obaid, Matthew Wetstein for team work and Professor Henry Frisch for the supervision.

Bibliography

[1] S. Davidson, E. Nardi, Y. Nir. *Leptogenesis*. Physics Reports, Vol. 466: pp. 105–177 (2008).

[2] S. F. King. *Neutrino mass models*. Reports of Progress in Physics, Vol. 67: pp. 107–157 (2004).

[3] http://psec.uchicago.edu

[4] http://en.wikipedia.org/wiki/Daniel_Boone

[5] http://www-boone.fnal.gov

[6] J. L. Wiza. *Microchannel plate detectors*. Nuclear Instruments and Methods, Vol. 162: pp. 587–601 (1979).

Appendix A

Muon motion in constant magnetic field in water

A.1 Muon energy loss in water

The muon energy losses in water can be described by the following formula

$$\epsilon = \frac{dE}{dx} = a\rho + b\rho E,$$

where ϵ is the energy loss rate, ρ is the density of water, E is the muon energy, and a and b are constants. For the range of the muon energy E about or below 1 GeV $a \approx 2$ MeV/(g/cm^2) and $b \approx 3 \cdot 10^{-6}$ cm^2/g. Taking into account that the density of water is $\rho = 1$ g/cm^3 one can notice that

$$a\rho \approx 2 \ \frac{\text{MeV}}{\text{cm}} \text{ and } b\rho E \leq 3 \cdot 10^{-3} \ \frac{\text{MeV}}{\text{cm}}.$$

This means that $a\rho \gg b\rho E$, and the energy loss rate can be expressed as

$$\epsilon \approx a\rho \approx 2 \ \frac{\text{MeV}}{\text{cm}}. \tag{A.1}$$

A.2 Muon 2D motion in constant magnetic field in vacuum

Let us consider a muon moving in water in constant magnetic field $\vec{B}$. At the initial moment of time the velocity direction of the muon is $\vec{\phi} \perp \vec{B}$. Let us introduce a coordinate system (x, y) such that magnetic field $\vec{B}$ is perpendicular to the plane (xy). In this coordinate system

$$\vec{\phi} = (\cos\phi, \sin\phi),$$

where ϕ is the angle between the vector $\vec{\phi}$ and x-axis. Note that $|\vec{\phi}| = 1$. The vector

$$\vec{n} = q(-\sin\phi, \cos\phi) \perp \vec{\phi}$$

is the normal vector. $q = \pm 1$ is the muon sign. The anti-radial vector is $\vec{R} = R\vec{n}$, where R is the radius of the curvature. ψ is a rotation angle. $\vec{\phi} + d\vec{\phi}$ is the muon velocity direction after rotation on the angle $d\psi$. Angles α, β, and γ are shown in Figure A.1.

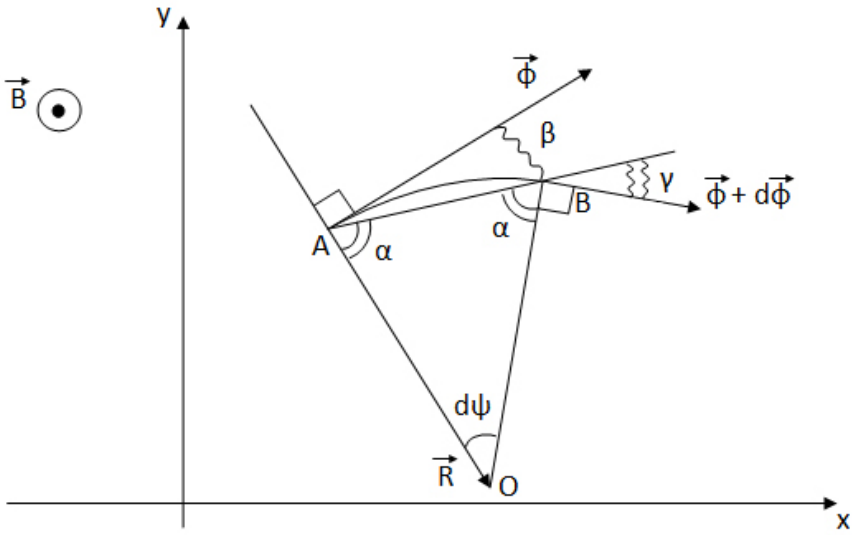

Figure A.1: The muon motion in constant magnetic field $\vec{B}$ perpendicular to the plane of the motion (xy). The plot is for a negatively charged muon.

From the triangle $\triangle AOB$

$$\alpha = \frac{\pi}{2} - \frac{d\psi}{2}.$$

Because of $\vec{n} \perp \vec{\phi}$

$$\beta = \frac{\pi}{2} - \alpha = \frac{d\psi}{2}.$$

From $\vec{\phi} + d\vec{\phi} \perp \overrightarrow{BO}$

$$\gamma = \pi - \frac{\pi}{2} - \alpha = \frac{d\psi}{2} = \beta.$$

Let us decompose the movement $\overrightarrow{AB} \equiv d\vec{x}$ in the basis of the vectors $\vec{\phi}$ and $\vec{n}$:

$$d\vec{x} = d\vec{x}_{\vec{\phi}} + d\vec{x}_{\vec{n}}. \tag{A.2}$$

By definition

$$d\vec{x}_{\vec{a}} = (\vec{a}, d\vec{x})\frac{\vec{a}}{|\vec{a}|}, \tag{A.3}$$

where $(\vec{a}, d\vec{x})$ is dot product of $\vec{a}$ and $d\vec{x}$. Note that

$$|d\vec{x}| = 2R\sin\frac{d\psi}{2},$$

$|\vec{\phi}| = 1$, and $|\vec{n}| = 1$. That is why[1]

$$(\vec{\phi}, d\vec{x}) = |\vec{\phi}| \cdot |d\vec{x}| \cos(\widehat{\vec{\phi}, d\vec{x}}) = 2R\sin\frac{d\psi}{2}\cos\beta = 2R\sin\frac{d\psi}{2}\cos\frac{d\psi}{2} = R\sin d\psi, \tag{A.4}$$

[1]The symbol $(\widehat{\vec{a}, \vec{b}})$ denotes the angle between the vectors $\vec{a}$ and $\vec{b}$.

$$(\vec{n}, d\vec{x}) = |\vec{n}| \cdot |d\vec{x}| \cos(\widehat{\vec{n}, d\vec{x}}) = 2R \sin \frac{d\psi}{2} \cos\alpha = 2R \sin^2 \frac{d\psi}{2} = R(1 - \cos d\psi). \tag{A.5}$$

From Equations (A.2), (A.3), (A.4), and (A.5) one can conclude that

$$d\vec{x} = (\vec{\phi}, d\vec{x})\vec{\phi} + (\vec{n}, d\vec{x})\vec{n} = \vec{\phi} R \sin d\psi + \vec{n} R(1 - \cos d\psi) = R\left[\vec{\phi} \sin d\psi + \vec{n}(1 - \cos d\psi)\right].$$

If $d\vec{x} = (dx, dy)$ then

$$dx = R\left[\cos\phi \sin d\psi - q \sin\phi(1 - \cos d\psi)\right], \tag{A.6}$$

$$dy = R\left[\sin\phi \sin d\psi + q \cos\phi(1 - \cos d\psi)\right], \tag{A.7}$$

The vector $\vec{\phi} + d\vec{\phi}$ is the muon velocity direction after the rotation on the angle $d\psi$. This means that $|\vec{\phi} + d\vec{\phi}| = 1$. That is why one can write that

$$\vec{\phi} + d\vec{\phi} = (\cos(\phi + d\phi), \sin(\phi + d\phi)). \tag{A.8}$$

It is clear from the Figure A.1 that

$$(\vec{\phi}, \widehat{\vec{\phi} + d\vec{\phi}}) = \beta + \gamma = d\psi.$$

Thus,

$$|d\phi| = d\psi. \tag{A.9}$$

To define the sign of $d\phi$ one should use the requirement

$$(\vec{n}, \vec{\phi} + d\vec{\phi}) > 0,$$

which means the trajectory is curved towards the vector $\vec{n}$ direction. From Equation (A.8)

$$\vec{\phi} + d\vec{\phi} = (\cos\phi \cos d\phi - \sin\phi \sin d\phi, \sin\phi \cos d\phi + \cos\phi \sin d\phi).$$

That is why

$$(\vec{n}, \vec{\phi} + d\vec{\phi}) = q(-\sin\phi \cos\phi \cos d\phi + \sin^2\phi \sin d\phi + \cos\phi \sin\phi \cos d\phi + \cos^2\phi \sin d\phi) = \\ = q \sin d\psi > 0 \Rightarrow q d\phi > 0.$$

This means that

$$q d\phi = d\psi. \tag{A.10}$$

If s is the path length, than $ds = R d\psi$. Finally, going back to Equations (A.6), (A.7), and (A.10), one can write a system of equations of motion as the following:

$$\begin{cases} q d\phi = d\psi, \\ ds = R d\psi, \\ dx = R\left[\cos\phi \sin d\psi - q \sin\phi(1 - \cos d\psi)\right], \\ dy = R\left[\sin\phi \sin d\psi + q \cos\phi(1 - \cos d\psi)\right]. \end{cases} \tag{A.11}$$

A.3 Muon 2D motion in constant magnetic field in water

A.3.1 Equations of motion

In the considered case muon energy losses rate does not depend on the muon energy (Equation (A.1)). That is why the muon energy in water changes according to the formula

$$E(s) = E_0 - \epsilon s, \tag{A.12}$$

where E_0 is the initial energy. The curvature radius depends on energy as

$$R(E(s)) = \frac{\sqrt{E^2(s) - m^2}}{cB},$$

where R is the curvature radius in meters, E is the muon energy in MeV, m is the muon mass in MeV, c is the speed of light, and B is the magnetic field in Tesla.

Based on the equations of motion in vacuum (A.11) one can write the differential equations of the muon motion in water assuming $d\psi \to 0$:

$$qd\phi = d\psi, \tag{A.13}$$

$$ds = R(E(s))d\psi, \tag{A.14}$$

$$dx = R(E(s))\cos\phi d\psi, \tag{A.15}$$

$$dy = R(E(s))\sin\phi d\psi. \tag{A.16}$$

First, let us consider Equation (A.13):

$$qd\phi = d\psi \Rightarrow \int_{\phi_0}^{\phi} qd\phi = \int_0^{\psi} d\psi \Rightarrow \phi = \phi_0 + \frac{\psi}{q}.$$

We can define the coordinate system such that $\phi_0 = 0$, then

$$\psi(\phi) = q\phi. \tag{A.17}$$

Also, note that

$$d\psi = qd\phi. \tag{A.18}$$

Now let us consider Equation (A.14):

$$ds = R(E(s))d\psi = \frac{\sqrt{E^2(s) - m^2}}{cB}d\psi \Rightarrow cB\frac{ds}{\sqrt{E^2(s) - m^2}} = d\psi.$$

From Equation (A.12) $dE = -\epsilon ds$. Thus,

$$-\frac{cB}{\epsilon}\frac{dE}{\sqrt{E^2 - m^2}} = d\psi \Rightarrow \int_0^{\psi} d\psi = -\frac{cB}{\epsilon}\int_{E_0}^{E}\frac{dE}{\sqrt{E^2 - m^2}} \Rightarrow \psi = \frac{cB}{\epsilon}\ln|E + \sqrt{E^2 - m^2}|\Big|_E^{E_0} \Rightarrow$$
$$\Rightarrow \ln\frac{E + \sqrt{E^2 - m^2}}{E_0 + \sqrt{E_0^2 - m^2}} = -\frac{\epsilon\psi}{cB} \Rightarrow$$
$$\Rightarrow \frac{E + \sqrt{E^2 - m^2}}{E_0 + \sqrt{E_0^2 - m^2}} = e^{-\frac{\epsilon\psi}{cB}}.$$

For convenience let us denote

$$\Psi = \frac{\epsilon\psi}{cB}. \tag{A.19}$$

Then

$$\frac{E + \sqrt{E^2 - m^2}}{E_0 + \sqrt{E_0^2 - m^2}} = e^{-\Psi}.$$

Let us introduce a variable $A_0 = E_0 + \sqrt{E_0^2 - m^2}$. In these terms

$$E + \sqrt{E^2 - m^2} = A_0 e^{-\Psi} \Rightarrow E = \frac{A_0}{2} e^{-\Psi} + \frac{m^2}{2A_0} e^{\Psi} = \frac{A_0}{2}\left(e^{-\Psi} + \rho^2 e^{\Psi}\right),$$

where

$$\rho = \frac{m}{A_0}.$$

Note that

$$E^2 - m^2 = \left[\frac{A_0}{2}\left(e^{-\Psi} - \rho^2 e^{\Psi}\right)\right]^2. \tag{A.20}$$

That is why one can write for the curvature radius the following formula:

$$R(\psi) = \frac{A_0}{2cB}\left[e^{-\Psi(\psi)} - \rho^2 e^{\Psi(\psi)}\right].$$

Using Equations (A.17) and (A.19) one can get

$$R(\phi) = \frac{A_0}{2cB}\left(e^{-k\phi} - \rho^2 e^{k\phi}\right), \tag{A.21}$$

where

$$k = \frac{q\epsilon}{cB}. \tag{A.22}$$

One can rewrite Equation (A.15) using Equations (A.17), (A.18), and (A.21) as

$$dx = \frac{qA_0}{2cB}\left(e^{-k\phi} - \rho^2 e^{k\phi}\right)\cos\phi d\phi \Rightarrow \int_{x_0}^{x} dx = \frac{qA_0}{2cB}\int_0^{\phi}\left(e^{-k\phi} - \rho^2 e^{k\phi}\right)\cos\phi d\phi.$$

Again, one can choose the coordinate system such that $x_0 = 0$. Then after the integration

$$x = \frac{qA_0}{2cB}\left(\int_0^{\phi} e^{-k\phi}\cos\phi d\phi - \rho^2\int_0^{\phi} e^{k\phi}\cos\phi d\phi\right). \tag{A.23}$$

One can show that

$$\int_0^{\phi} e^{k\phi}\cos\phi d\phi = \frac{e^{k\phi}(\sin\phi + k\cos\phi) - k}{1 + k^2}.$$

Thus,

$$x = \frac{qA_0}{2cB}\left[\frac{e^{-k\phi}(\sin\phi - k\cos\phi) + k}{1 + k^2} - \rho^2\frac{e^{k\phi}(\sin\phi + k\cos\phi) - k}{1 + k^2}\right];$$

$$x = C\left[k(1 + \rho^2) - k(e^{-k\phi} + \rho^2 e^{k\phi})\cos\phi + (e^{-k\phi} - \rho^2 e^{k\phi})\sin\phi\right],$$

where

$$C = \frac{qA_0}{2cB}\frac{1}{1+k^2}.$$

Similar calculations can be done for Equation (A.16).

$$dy = \frac{qA_0}{2cB}\left(e^{-k\phi} - \rho^2 e^{k\phi}\right)\sin\phi d\phi \Rightarrow y = \frac{qA_0}{2cB}\left(\int_0^\phi e^{-k\phi}\sin\phi d\phi - \rho^2\int_0^\phi e^{k\phi}\sin\phi d\phi\right), \quad \text{(A.24)}$$

where one assumes $y_0 = 0$. One can show that

$$\int_0^\phi e^{k\phi}\sin\phi d\phi = \frac{1 + e^{k\phi}(k\sin\phi - \cos\phi)}{1+k^2}.$$

Finally,

$$y = C\left[(1-\rho^2) - (e^{-k\phi} - \rho^2 e^{k\phi})\cos\phi - k(e^{-k\phi} + \rho^2 e^{k\phi})\sin\phi\right].$$

Taking into account Equation (A.17) and the fact that $|q| = 1$, one can write the solutions for (A.15) and (A.16) as

$$x(\psi) = C\left[k(1+\rho^2) - k(e^{-qk\psi} + \rho^2 e^{qk\psi})\cos\psi + q(e^{-qk\psi} - \rho^2 e^{qk\psi})\sin\psi\right], \quad \text{(A.25)}$$

$$y(\psi) = C\left[(1-\rho^2) - (e^{-qk\psi} - \rho^2 e^{qk\psi})\cos\psi - qk(e^{-qk\psi} + \rho^2 e^{qk\psi})\sin\psi\right].$$

One can see the graphical representation of the solution in Figure 2.1.

A.3.2 Maximum rotation angle

Let us define the maximum value of the rotation angle $\psi_{\max}$ as the angle when kinetic energy of the muon becomes zero. Thus the condition for the maximum rotation angle is $E = m$. According to Equation (A.20) this means that

$$\frac{A_0}{2}\left(e^{-\Psi_{\max}} - \rho^2 e^{\Psi_{\max}}\right) = 0 \Rightarrow e^{-\Psi_{\max}} = \rho^2 e^{\Psi_{\max}} \Rightarrow e^{-2\Psi_{\max}} = \rho^2 \Rightarrow \Psi_{\max} = \ln\frac{1}{\rho}.$$

From Equation (A.19)

$$\Psi_{\max} = \ln\frac{1}{\rho} \Rightarrow \frac{\epsilon\psi_{\max}}{cB} = \ln\frac{1}{\rho} \Rightarrow \psi_{\max} = \frac{cB}{\epsilon}\ln\frac{1}{\rho}.$$

Note, that the trajectory in Figure 2.1 is shown for the rotation angle in the range from 0 to $\psi_{\max}$.

A.3.3 Sagitta position

Sagitta is the maximum deviation of the trajectory from the line connecting the initial and the final points of the trajectory. Sagitta of the muon trajectory is a parameter which defines the necessary resolution of the detectors. Let us find a point where this deviation happens. The vector from the initial point of the trajectory to its final point is

$$\vec{L} = \vec{x}(\psi_0) = (x(\psi_0), y(\psi_0)).$$

Remember, that the coordinate system is chosen the way that $\vec{x}(0) = \vec{0}$. The normal vector to $\vec{L}$ is

$$\vec{N} = (-y(\psi_0), x(\psi_0)) \perp \vec{L}.$$

The distance between a point of the trajectory $\vec{x}(\psi)$ and the line connecting initial and final points of the trajectory is

$$d = \frac{|(\vec{x}(\psi), \vec{N})|}{|\vec{N}|}. \tag{A.26}$$

To find the point with maximum d one needs to solve the equation for $\tilde{\psi}$

$$\frac{d}{d\psi}(\vec{x}(\psi), \vec{N})\Big|_{\psi=\tilde{\psi}} = 0.$$

Taking into account that $\vec{x}(\psi) = (x(\psi), y(\psi))$ one can write

$$\frac{d}{d\psi}(\vec{x}(\psi), \vec{N})\Big|_{\psi=\tilde{\psi}} = x(\psi_0)\frac{dy(\tilde{\psi})}{d\psi} - \frac{dx(\tilde{\psi})}{d\psi}y(\psi_0) = 0.$$

From Equations (A.23) and (A.24), using Equation (A.18):

$$\begin{aligned}\frac{dx(\tilde{\psi})}{d\psi} = \frac{1}{q}\frac{dx(\tilde{\phi})}{d\phi} = \frac{1}{q}\,\frac{d}{d\phi}\left[\frac{qA_0}{2cB}\left(\int_0^{\phi} e^{-k\phi}\cos\phi d\phi - \rho^2\int_0^{\phi} e^{k\phi}\cos\phi d\phi\right)\right]\Bigg|_{\phi=\tilde{\phi}} = \\ = \frac{A_0}{2cB}\left(e^{-k\tilde{\phi}} - \rho^2 e^{k\tilde{\phi}}\right)\cos\tilde{\phi} = \frac{A_0}{2cB}\left(e^{-qk\tilde{\psi}} - \rho^2 e^{qk\tilde{\psi}}\right)\cos\tilde{\psi};\end{aligned}$$

$$\begin{aligned}\frac{dy(\tilde{\psi})}{d\psi} = \frac{1}{q}\frac{dy(\tilde{\phi})}{d\phi} = \frac{1}{q}\,\frac{d}{d\phi}\left[\frac{qA_0}{2cB}\left(\int_0^{\phi} e^{-k\phi}\sin\phi d\phi - \rho^2\int_0^{\phi} e^{k\phi}\sin\phi d\phi\right)\right]\Bigg|_{\phi=\tilde{\phi}} = \\ = \frac{A_0}{2cB}\left(e^{-k\tilde{\phi}} - \rho^2 e^{k\tilde{\phi}}\right)\sin\tilde{\phi} = \frac{A_0}{2cB}\left(e^{-qk\tilde{\psi}} - \rho^2 e^{qk\tilde{\psi}}\right)\sin(q\tilde{\phi}).\end{aligned}$$

That is why

$$\begin{aligned}x(\psi_0)\left(e^{-qk\tilde{\psi}} - \rho^2 e^{qk\tilde{\psi}}\right)\sin(q\tilde{\phi}) - y(\psi_0)\left(e^{-qk\tilde{\psi}} - \rho^2 e^{qk\tilde{\psi}}\right)\cos\tilde{\psi} = 0 \Rightarrow \\ \Rightarrow \left(e^{-qk\tilde{\psi}} - \rho^2 e^{qk\tilde{\psi}}\right)\left[x(\psi_0)\sin(q\tilde{\phi}) - y(\psi_0)\cos\tilde{\psi}\right] = 0 \Rightarrow \\ \left[\begin{array}{l} e^{-qk\tilde{\psi}} - \rho^2 e^{qk\tilde{\psi}} = 0, \\ x(\psi_0)\sin(q\tilde{\phi}) - y(\psi_0)\cos\tilde{\psi} = 0 \end{array}\right. \Rightarrow \left[\begin{array}{l} \tilde{\psi} = \dfrac{1}{qk}\ln\dfrac{1}{\rho}, \\ \dfrac{\sin(q\tilde{\phi})}{\cos\tilde{\psi}} = \dfrac{y(\psi_0)}{x(\psi_0)}. \end{array}\right.\end{aligned}$$

Because of $|q| = 1$ and Equation (A.22)

$$\tilde{\psi} = \frac{1}{qk}\ln\frac{1}{\rho} = \frac{cB}{q^2\epsilon}\ln\frac{1}{\rho} = \frac{cB}{\epsilon}\ln\frac{1}{\rho} = \psi_{\max}.$$

This is a singular point, but not a solution. Due to $|q| = 1$

$$\frac{\sin(q\tilde{\phi})}{\cos\tilde{\psi}} = \frac{y(\psi_0)}{x(\psi_0)} \Rightarrow \frac{q\sin(\tilde{\phi})}{\cos\tilde{\psi}} = \frac{y(\psi_0)}{x(\psi_0)} \Rightarrow \tan\tilde{\psi} = q\frac{y(\psi_0)}{x(\psi_0)}.$$

A.3.4 Rotation angle dependence on traveled distance

Suppose the muon flew a distance x_0 in x-direction. One can estimate the rotation angle for this trajectory based on Equation (A.25):

$$x_0 = x(\psi_0) = C\left[k(1+\rho^2) - k(e^{-qk\psi_0} + \rho^2 e^{qk\psi_0})\cos\psi_0 + (e^{-qk\psi_0} - \rho^2 e^{qk\psi_0})\sin(q\psi_0)\right].$$

Let us use the following approximations.

- $\rho^2 \ll 1$. For the case of the muon energy of 1 GeV $\rho \approx 0.053$. The approximate equation will be

  $$x_0 = C\left[k - ke^{-qk\psi_0^*}\cos\psi_0^* + e^{-qk\psi_0^*}\sin(q\psi_0^*)\right] \overset{|q|=1}{\Longrightarrow} \frac{x_0}{C} - k = e^{-qk\psi_0^*}\left(q\sin\psi_0^* - k\cos\psi_0^*\right).$$

  The solution for the case of 1 GeV muon energy, 100 gauss magnetic field and $q = 1$ is

  $$\psi_0^* = 7.7 \cdot 10^{-3} \text{ rad}.$$

- $\psi_0^* \ll 1 \Rightarrow \sin\psi_0^* \ll \cos\psi_0^*$. Besides $|k| \gg 1$. For the considered case $|k| \approx 67$. It gives us an approximation:

  $$\frac{x_0}{C} - k = e^{-qk\psi_0^*}\left(q\sin\psi_0^* - k\cos\psi_0^*\right) \approx -ke^{-qk\psi_0^*}\cos\psi_0^*.$$

- $|\psi_0^*| \ll 1 \Rightarrow \cos\psi_0^* \approx 1$. The approximate equation is

  $$\frac{x_0}{C} - k = -ke^{-qk\psi_0^*} \Rightarrow \psi_0^* = -\frac{1}{qk}\ln\left(1 - \frac{x_0}{Ck}\right) \tag{A.27}$$

  is our final estimation.

To check the estimation one can build a function

$$x_0^*(x_0) = x(\psi_0^*(x_0)) = C\left\{k(1+\rho^2) - k\left(1 - \frac{x_0}{Ck} + \rho^2\frac{1}{1-\frac{x_0}{Ck}}\right)\cos\left[\frac{1}{k}\ln\left(1-\frac{x_0}{Ck}\right)\right] + \right.$$
$$\left. + \left(1 - \frac{x_0}{Ck} - \rho^2\frac{1}{1-\frac{x_0}{Ck}}\right)\sin\left[\frac{q}{k}\ln\left(1-\frac{x_0}{Ck}\right)\right]\right\}. \tag{A.28}$$

One can see (Figure A.2) that this function is almost linear. To examine the estimation more precisely should study the absolute error $f(x_0) = x_0^*(x_0) - x_0$ and the relative error

$$\delta(x_0) = \frac{|f(x_0)|}{x_0}.$$

It is clear from Figure A.3 that in the range of traveled distance up to 3 m the absolute error of the estimation is beyond a few centimeters, which delivers (Figure A.4) the relative error less than 1%. That is why one can use the approximation (A.27) of the rotation angle for traveled distance x_0.

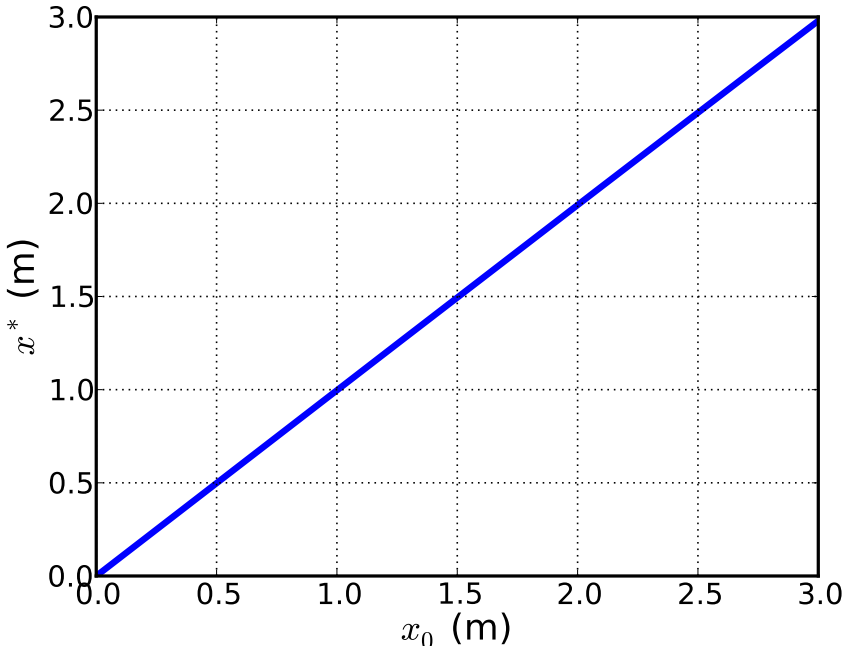

Figure A.2: The estimation (A.28) of x_0 value dependence on x_0 for the magnetic field $B = 100$ gauss.

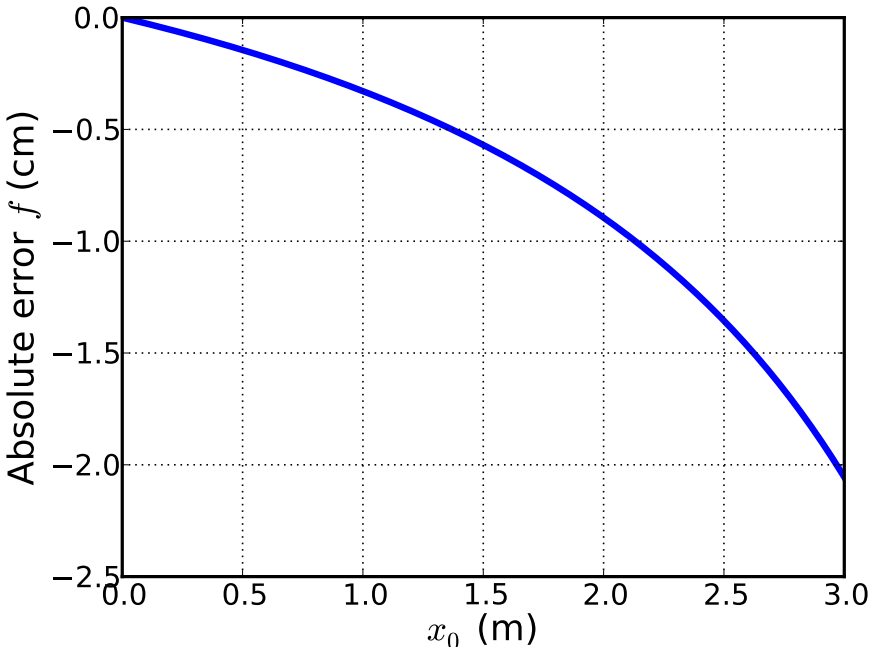

Figure A.3: The absolute error of the estimation (A.28) of x_0 value dependence on x_0 for the magnetic field $B = 100$ gauss.

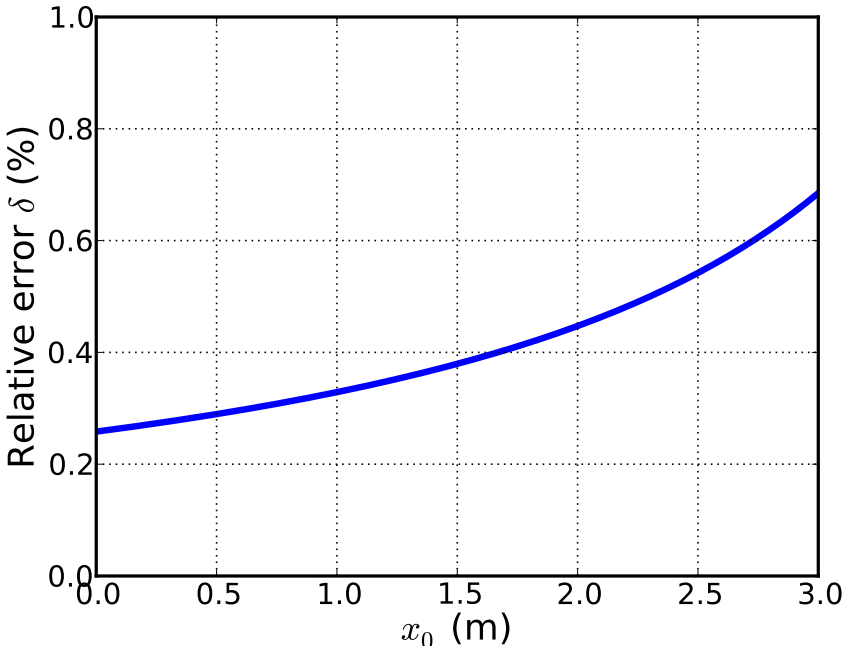

Figure A.4: The relative error of the estimation (A.28) of x_0 value dependence on x_0 for the magnetic field $B = 100$ gauss.

Sagitta value

Based on Equation (A.26) the sagitta value can be defined by the following formula:

$$d = \frac{|x(\psi_0)y(\tilde{\psi}) - x(\tilde{\psi})y(\psi_0)|}{\sqrt{x^2(\psi_0) + y^2(\psi_0)}}.$$

Using the estimation derived above one can find that the sagitta value depends linearly on the strength of the magnetic field (Figure 2.3) and quadratically on the traveled distance x_0 (Figure **??**).